AIAA Journal
Vol. 44, No. 1, January 2006

Combustion Enhancement via Stabilized Piecewise Nonequilibrium Gliding Arc Plasma Discharge

Timothy Ombrello,* Xiao Qin,[†] and Yiguang Ju[‡]
Princeton University, Princeton, New Jersey 08544
Alexander Gutsol[§] and Alexander Fridman[¶]
Drexel University, Philadelphia, Pennsylvania 19104
and
Campbell Carter**
U.S. Air Force Research Laboratory, Wright–Patterson Air Force Base, Ohio 45433

A new piecewise nonequilibrium gliding arc plasma discharge integrated with a counterflow flame burner was developed and validated to study the effect of a plasma discharge on the combustion enhancement of methane–air diffusion flames. The results showed that the new system provided a well-defined flame geometry for the understanding of the basic mechanism of the plasma–flame interaction. It was shown that with a plasma discharge of the airstream, up to a 220% increase in the extinction strain rate was possible at low-power inputs. The impacts of thermal and nonthermal mechanisms on the combustion enhancement was examined by direct comparison of measured temperature profiles via Rayleigh scattering thermometry and OH number density profiles via planar laser-induced fluorescence (calibrated with absorption) with detailed numerical simulations at elevated air temperatures and radical addition. It was shown that the predicted extinction limits and temperature and OH distributions of the diffusion flames, with only an increase in air temperature, agreed well with the experimental results. These results suggested that the effect of a stabilized piecewise nonequilibrium gliding arc plasma discharge of air at low air temperatures on a diffusion flame was dominated by thermal effects.

Nomenclature

a = strain rate of the counterflow flame
B = magnetic field
C_d = drag coefficient
d = arc surface area
F_a = ampere force per unit arc length
F_d = drag force
I = current
i, j = indices representing the two nozzles streams
L = distance between counterflow nozzles
Q = volumetric flow rate
u = gas velocity
ρ = gas density

I. Introduction

THE quest for practical high-speed airbreathing propulsion systems has been a subject of much attention for almost a half of a century in the world of aerospace and aeronautics. From the initial designs of ramjets and supersonic combustion ramjets, there have been significant advancements over this period of time, bringing us closer to a reliable system. Two of the most critical issues in developing these systems have come in the form of ignition and stabilization of the flame in the propulsion device. This is because of the flow speed being so high, leaving only a very short residence time from initiation to completion for combustion reactions.

Many different approaches have been put forth to combat these problems, from changing the geometry of the combustor to adding additional energy to the system. From the standpoint of geometric changes, cavities or struts can be added to the wall of the combustor to provide better mixing, longer residence time, and subsonic regions necessary for anchoring and stabilization of the flame.[1–5] These passive methods primarily provide enhancement by increasing mixing or creating a low-speed region of the flow to allow for flameholding and stabilization. To go hand-in-hand with cavities, the method of precombustion can be used in these isolated parts of the flow in a cavity or in a separate combustion chamber.[6–8] Here, the heat and products of the combustion have proven to be an effective means of decreasing the ignition time and increasing the flame stabilization. However, one practical problem with this approach is the requirement of the additional combustion chamber (and perhaps additional fuel and air for that chamber). Furthermore, there is also the constraint of the flammability limits of the fuel in the precombustor, especially for hydrocarbon fuels.

An attractive means to resolve these problems comes in the form of plasma-enhanced combustion. Many forms of plasma have been developed for this duty and have shown significant enhancement.[9–15] When looking at all of these different types of plasma systems, two questions may arise. First, what is the optimal type of plasma system? Second, how does it work to enhance the combustion? The types of plasma and their benefits first need to be discussed. Plasmas can be categorized as either thermal or nonthermal, that is, nonequilibrium. Thermal plasmas include arc discharges, plasma torches, and radio frequency inductively coupled plasmas. They mainly ionize and dissociate the reactants thermally, leading to large amounts of joule heating. Because of this heat addition, the gas temperatures are very high (5000–50,000 K), with electron temperatures of the same order and energy input in all degrees

---

Presented as Paper 2005-1194 at the AIAA 43rd Aerospace Sciences Meeting, Reno, NV, 10–13 January 2005; received 7 April 2005; revision received 19 August 2005; accepted for publication 22 August 2005.

*Graduate Student, Department of Mechanical and Aerospace Engineering, Engineering Quadrangle on Olden Street. Student Member AIAA.

[†] Research Staff, Department of Mechanical and Aerospace Engineering, Engineering Quadrangle on Olden Street. Member AIAA.

[‡] Assistant Professor, Department of Mechanical and Aerospace Engineering, Engineering Quadrangle on Olden Street. Associate Fellow AIAA.

[§] Research Professor, Drexel Plasma Institute, 34th and Lancaster Avenue. Member AIAA.

[¶] Professor, Drexel Plasma Institute, 34th and Lancaster Avenue. Member AIAA.

**Senior Aerospace Engineer, Aerospace Propulsion Division. Associate Fellow AIAA.

of freedom. This results in poor chemical reaction selectivity, just increasing all of the reaction rates due to the elevated temperatures. Furthermore, there would be either large power requirements or localized activation such as with a plasma jet, for example, only penetrating into a small portion of a transverse supersonic flow. Nonequilibrium plasmas, which include low-pressure glow, radio frequency, corona, microwave, and nanosecond high-voltage discharges, have the benefit of high chemical selectivity and homogeneous activation. The primary means of dissociation and ionization is direct electron impact from high-temperature (-speed) electrons accelerated by a high electric field. The homogeneous activation leads to power requirements that can become extremely high, sometimes in excess of several kilowatts. Therefore, an ideal plasma discharge should have intermediate temperatures between that of a thermal and nonthermal discharge, which is high enough for the ignition of the mixture, and the activation benefits of a homogeneous discharge, providing high levels of chemical reaction selectivity, high electron temperatures, and high electron densities with low-power requirements.[16]

Once the criteria for an ideal discharge have been established, the next step is to understand at what conditions and to what extent there will be thermal and nonthermal effects. For ignition, it is very clear that radical addition will shorten the ignition time. However, for flame stabilization and burning rates, it has long been debated whether there is a nonthermal effect in plasma-assisted combustion.[9,10] The main factor that complicates the answer to this question is the complexity of a plasma discharge and the flowfield. Therefore, to understand the nonthermal and thermal effects at specific conditions, the plasma system has to be simplified and integrated with a flow system so that the interaction between the flow and flame can be isolated and that the detailed mechanism of the interaction between the flame and the plasma can be well understood. Therefore, it is particularly important to design a simplified combustion device for nonequilibrium plasma-assisted combustion enhancement so that the effects of nonequilibrium plasma on a flame can be observed and to what extent those effects are thermal and/or nonthermal can be understood.

The present research is motivated by the preceding discussion. The goal of this research was to develop an ideal and simplified plasma discharge using piecewise activation for minimal power consumption and the integration with a counterflow burner to understand the fundamental interaction between nonequilibrium plasma and diffusion flames. This was accomplished by first designing a stabilized nonequilibrium gliding arc plasma discharge system to provide piecewise activation. Then by the integration of this plasma system with a counterflow burner, a simple platform was established to study the plasma flame interaction. This included experimental studies of the extinction behavior, laser diagnostics for flame temperatures via planar Rayleigh scattering and OH number densities via OH planar laser-induced fluorescence (PLIF). These results were then compared to numerical computations using detailed chemistry to validate the measurements and clarify the roles of thermal and nonthermal effects in nonequilibrium plasma-assisted combustion.

II. Apparatus

A. Piecewise Discharge Plasma System

1. *Gliding Arc*

The stabilized gliding arc is a special type of electrical discharge that occurs between two diverging high-voltage electrodes and has both thermal and nonthermal plasma merits. The arc is first established when a sufficiently high enough potential is applied across the electrodes (approximately 3 kV/mm in air) to break down the gas at the smallest gap. Once a conductive channel is established (arc), the current very rapidly increases while the voltage decreases simultaneously to maintain the discharge. This is a thermal plasma, with thermal dissociation and ionization being the primary means of maintaining the arc discharge with a low voltage and high current. The arc then moves downstream due to the buoyancy and/or flow, elongating as the gap between the electrodes increases. During this process, the arc continually loses heat to the surroundings because of the increased arc surface area. The voltage is also continually increasing while the current is simultaneously decreasing to maintain a constant power. At a point when the arc elongates such that the power supplied to the source cannot balance the amount of heat lost to the surroundings, the arc makes a transition to a nonequilibrium regime. The primary means of dissociation and ionization is then due to direct electron impact from high-temperature electrons accelerated by the higher electric field. This part of the gliding arc discharge, in the nonequilibrium regime, has the important benefit of lower gas temperature to provide better chemical selectivity. The arc then continues to elongate as it propagates along the diverging electrodes until it finally extinguishes. Once there is a sufficiently high potential built up between the electrodes, the process starts again, being cyclic in nature.

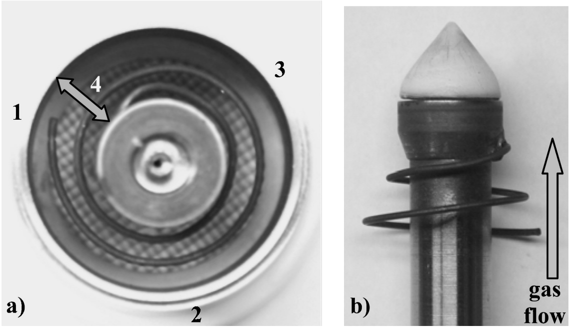

Fig. 1 Gliding arc plasma system: path of the gliding arc from initiation, point 1, to arc rotation/elongation, points 2 and 3, and finally arc stabilization, point 4: a) top view of system and b) side view of central electrode.

Unfortunately in a gliding arc system, the nonequilibrium regime exists only for a short period of time in the arc evolution process. Recently, however, it was found that during the gliding arc process, the arc can be stabilized well past the transition from the thermal equilibrium to the nonequilibrium regime before extinction.[17] This is significant because the process would not have to be cyclic, like a traditional gliding arc, to observe the benefits for a small nonequilibrium portion of the process of each cycle. Because of this newfound stability, the plasma arc can be stabilized near extinction in the nonequilibrium regime for an indefinite amount of time, creating a plasma disk. This study utilizes this special type of gliding arc discharge. As seen in Fig. 1, it comprises a stainless-steel inner and outer electrode, which is the cathode and the anode (as well as the ground), respectively. There is a wire attached to the cathode that is separated from the outer anode by 2 mm at the smallest gap (point 1, Fig. 1). The wire spirals progressively closer to the cathode to where it is attached, which is at the largest gap between the two electrodes. In addition, there is a magnetic field in the discharge region produced by an external donut-shaped permanent ceramic magnet. The direction of the magnetic field determines the direction of the rotation of the arc (in this case counterclockwise to follow the wire when looking down upon the system as in Fig. 1), and the field strength, as well as the power input, determines the frequency of rotation.

2. *Plasma Disk*

When a high voltage is applied to the plasma device, there is an initial breakdown of the feedstock at the smallest gap and a thermal plasma is established. The arc then rotates in the magnetic field and increases in length as the distance between the spiraled wire and the outer electrode increases (Fig. 1, from point 1 to point 2 to point 3). The increased length of the arc results in a transition to a nonequilibrium plasma leading to more rapid cooling and intermediate temperatures (2000–3000 K), as well as an increased electric field and electron temperature (>1 eV). Once the arc reaches the cylindrical inner electrode (point 4, Fig. 1), there is a stable rotating intermediate temperature arc in the gas flow. A top view of this plasma disk can be seen in Fig. 2. The plasma arc rotation frequency ranges from approximately 20 to 50 Hz and only decreases by a few percent when the flow rate is increased (Fig. 3). The increased

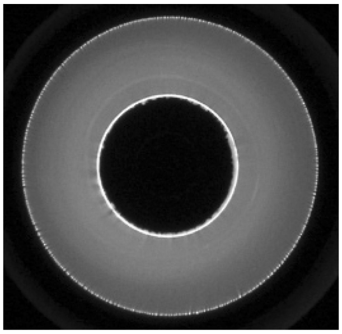

Fig. 2 Top view of plasma disk.

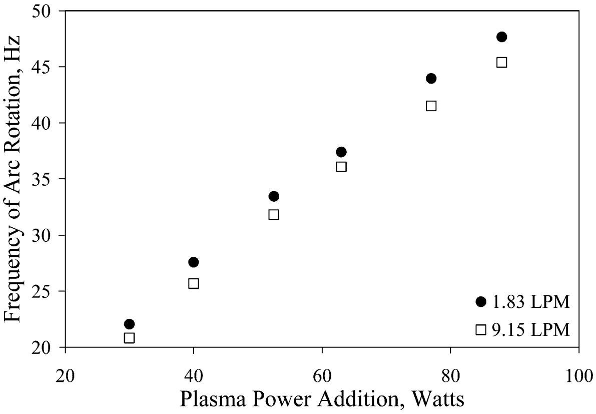

Fig. 3 Frequency of arc rotation for two airflow rates.

rotation frequency comes from the higher current input (and, hence, higher power addition), forcing the arc to rotate faster in the magnetic field. When the arc reaches the largest gap, it remains at a fixed axial position with a constant length as it rotates. This is because the arc is no longer convecting downstream. It maintains itself there because it is rotating through media that was previously ionized, not through the initial nonionized gas. Therefore, it requires less power for the arc to remain at that position as opposed to quenching and reinitiating at the smallest electrode gap.

Because the frequency of rotation of the arc is fast when compared to the gas velocity, there is quasi-uniform activation of the flow. To show this, calculations were performed to find what flow rate Q of air could be quasi uniformly activated by the gliding arc. The system had a distance of 10 mm at the largest gap where the plasma disk was located and a magnetic field B of 0.15 T (a typical value that is possible to obtain with permanent ceramic magnets). The low-current, high-voltage gliding arc operation would have an electric field strength E for the case of the gliding arc propagation through nonionized air of about 0.1 kV/mm. This would lead to a gliding arc voltage drop of 1 kV for the given length of the gap. The ampere force per unit of arc length that would rotate the gliding arc would be $F_a = IB$, and when in equilibrium conditions, it would be equal to the drag force F_d. It was possible to estimate the drag force per unit length from the assumption that all of the gas was flowing around the high-temperature cylinder of the arc. The drag force on the cylinder can be calculated as $F_d = 0.5\, C_d \rho d u^2$. The limits for the drag coefficient for a very wide range of Reynolds numbers (from 10^2 to 10^5) are $1.3 < C_d < 1$, and thus,[18]

$$\tfrac{1}{2} C_d \rho d u^2 = IB \tag{1}$$

Therefore, the arc, which was approximately 2 mm in diameter, moved relative to the gas flow along a spiral trajectory, and if the gas velocity $u < d/\tau$, then all of the gas flow would be uniformly treated by the arc. For the plasma system, this corresponded to $u <$ 4–10 cm/s and $Q <$ 35–88 cm^3/s for the range of powers used. In addition to the direct treatment by the rotating gliding arc, all of the gas flow would pass through the ionized disk that the gliding arc left behind.

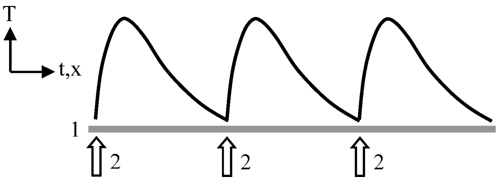

Fig. 4 Piecewise discharge concept: 1) quenching limit of a flame and 2) points of plasma discharge.

This plasma disk, which would allow a quasi-uniform activation of the flow, can be thought of as a piecewise discharge in terms of space or time. For example, in Fig. 4, it can be seen in a temperature vs time or spatial coordinate plot, if there is a discharge, providing a source of some heat and/or radicals, the gas temperature will rise due to the combustion process, but then will decrease if the conditions are not satisfactory for the survival of the combustion process. If no more energy is added, the flame will extinguish, but if there is another discharge before that (within the quenching distance or time), the flame will survive. This can be continually done, sustaining the burning of the flame.

To produce this gliding arc discharge, a power supply was specifically created to supply efficiently the needs of the gliding arc system stabilized by the magnetic field. It was designed to produce a magnetically stabilized arc with minimum current while maintaining smooth current regulation. This was accomplished by minimizing the active energy losses by using a reactive capacitive resistance that imitated the resistive voltage and current characteristics. To minimize the output electric capacity and to provide the voltage–current characteristic of the power supply (which is close to the resistive voltage–current characteristics), changing the frequency of the high-voltage converter allowed variation of the virtual resistance. After the output rectifier, there was unidirectional voltage and current with a very high frequency of the residual pulsation. The plasma arc behavior was then the same as that for the plasma arc at a constant current and voltage because of the limited time response of the gliding arc.

B. Counterflow Flame Burner Integration

To provide an ideal platform to integrate the stabilized gliding arc plasma discharge with a combustion system, the counterflow flame burner was chosen. The counterflow system provides four key benefits of minimal buoyancy effects, simplified flame geometry, ability to define a flow velocity gradient (strain rate or inverse of residence time) on the centerline near the stagnation plane of the two impinging jets, defined as[19–23]

$$a_i = (2v_i/L)\left[1 + (v_j/v_i)\sqrt{\rho_j/\rho_i}\right] \tag{2}$$

and, last, excellent optical access for advanced laser diagnostics for species and temperature measurements.

A schematic of the system is shown in Fig. 5. The system consists of two converging nozzles 15 mm in diameter, separated by 13 mm. The upper nozzle was water cooled. The feedstock for the plasma device, upstream of the lower nozzle, was air, whereas nitrogen-diluted methane flowed through the upper nozzle. To isolate the flame from the ambient air and disturbances, a nitrogen "curtain" was used. The nitrogen curtain passed through a 0.75-mm annular slit around the circumference of each nozzle exit. The velocity of the curtain was maintained at or below the exit speed of the nozzle to minimize diffusion into the stream. The flame was established on the upstream air side of the stagnation plane. This system allowed for the examination of the effects of stretch on the quenching limit of the flame as a function of the flow velocity gradient for different levels of plasma power addition.

The flow rates of the individual gases were controlled with sonic nozzles that were calibrated with a DryCal dry piston flow meter (1% error). The methane and nitrogen were then mixed in a hollow mixing cylinder (for minimal backpressure). To ensure that the mixture input to the flame was held constant while the velocity was increased through the nozzles, a bypass system was used. Here, the

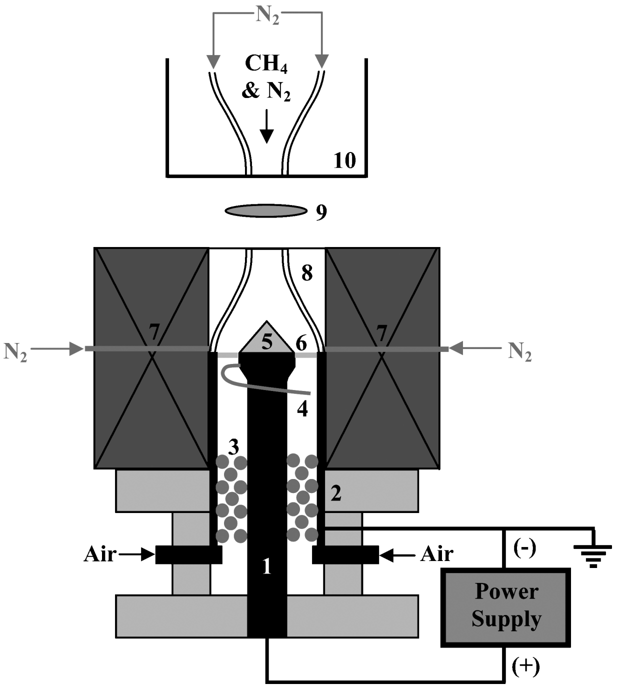

Fig. 5 Counterflow burner with integrated plasma system: 1) cathode, 2) anode, 3) diffuser, 4) gliding arc initiation wire, 5) insulator, 6) plasma disk, 7) magnet, 8) converging nozzle with N_2 curtain, 9) flat diffusion flame, and 10) water-cooled converging nozzle with N_2 curtain.

methane–nitrogen mixture, as well as the air, was teed off before the respective nozzles. The flow rate could then be increased or decreased through the nozzles by closing or opening the valves of the bypasses, respectively. By then measuring the flow through the bypass using the DryCal flow meter, the nozzle exit velocities could be calculated.

To find the extinction limits, the flame was first established with the bypass fully open and, hence, the lowest flow rate through the nozzles (and strain exerted on the flame). Then each bypass was slowly closed, while maintaining the stagnation plane at a fixed position. During this process, the flame moved closer to the stagnation plane between the two nozzles, which decreased the residence mixing time as well as increased the strain rate until flame extinction.

Two photographs of the nitrogen-diluted methane–air counterflow flames with and without plasma power addition can be seen in Fig. 6. Note the one-dimensional structure of the flame. In all cases, the flame was very steady and had minimal curvature, providing an excellent platform to perform experimental measurements via laser diagnostics and geometry that was easy to reproduce computationally. There was also a difference in luminosity between the flame with (Fig. 6a) and without (Fig. 6b) plasma activation of the airstream. The flame with plasma activation of the air has a larger luminous zone with a distinct white and orange coloring as compared to the typical bright blue of the nonactivated flame. This indicates that there is an effect of the stabilized piecewise gliding arc plasma discharge on the diffusion flame.

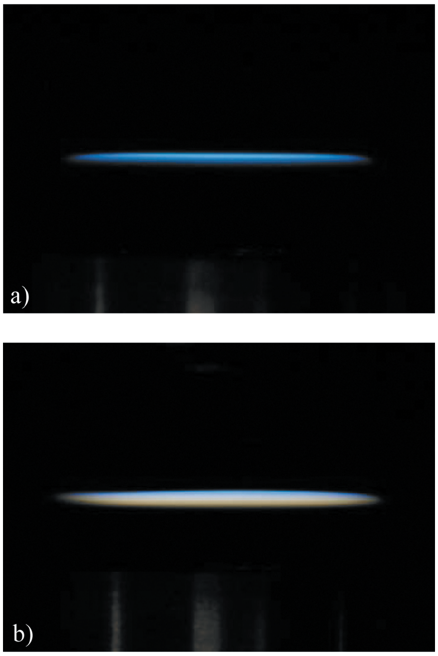

Fig. 6 Methane–air counterflow diffusion flames at strain rate of 298.5 s^{-1}: a) no plasma power addition and b) 60 W of plasma power addition.

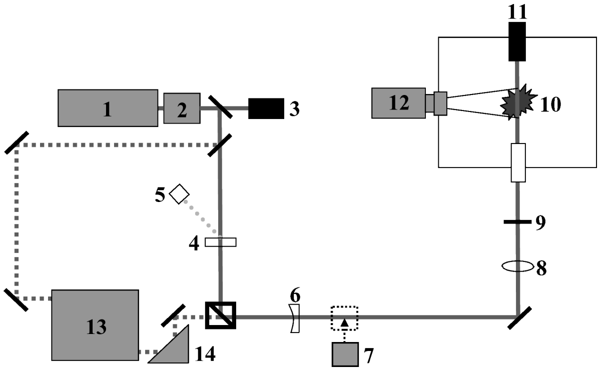

Fig. 7 Planar Rayleigh scattering and OH PLIF setup: 1) injection seeded Nd:YAG laser, 2) frequency doubler, 3) beam dump, 4) half-wave plate, 5) diode energy meter, 6) lens, 7) power meter, 8) lens, 9) clipper, 10) flame, 11) beam dump, 12) ICCD camera, 13) dye laser with frequency doubler, and 14) Pellin–Broca prism.

C. Rayleigh Scattering and OH PLIF

To measure the temperature profiles of the diffusion flame between the two nozzles, a Rayleigh scattering system was utilized (Fig. 7). A frequency-doubled, injection-seeded Nd:YAG laser (Quanta-Ray GCR-4) with an output of approximately 450 mJ/pulse was used. For OH measurements, the OH was excited via a Lumonics HD-300 dye laser pumped with the Nd:YAG laser already described (Fig. 7). The wavelength was tuned to 567.106 nm so that the frequency-doubled radiation matched the wavelength for the $Q_1(8)$ transition of the $A^2\Sigma^+$–$X^2\Pi$ (1,0) band; the Boltzmann population fraction of the ground state ($N = 8$) reaches a maximum near 1600 K and varies little over the temperature range of 1200–2200 K; for example, $f_B(2200\,\mathrm{K})/f_B(1600\,\mathrm{K}) = 0.934$. The resulting pump linewidth was approximately 0.1 cm^{-1}, whereas the 283-nm beam energy was 12 mJ/pulse. The beam energy was measured and recorded for each image taken by directing a small portion of the beam (either 532 or 283 nm) to a photodiode (or Molectron Joulemeter). For both temperature and OH measurements, a laser sheet was formed using two lenses. These consisted of a plano–concave cylindrical lens (−300-mm focal length) to spread the beam in the vertical direction and a plano–convex spherical lens (1-m focal length) to focus the beam in the horizontal direction and also collimate the beam in the vertical direction. The laser sheet was then directed between the two nozzles of the counterflow flame burner. To define clearly the laser sheet and minimize any stray scattering in the vertical direction, absorptive filters were used to "clip" the sheet. The scattering was imaged with a Princeton Instruments PIMAX intensified charge-coupled device (ICCD) camera (one with a photocathode optimized for the visible spectrum for Rayleigh scattering and one for the UV spectrum for OH fluorescence). For Rayleigh scattering, a Nikon 105-mm, ƒ/2.8 macrolens was used, whereas for OH PLIF, a Nikon UV Nikkor 105 mm ƒ/4.5 lens was used along with UG-11 and WG-295 Schott glass filters to isolate fluorescence from the A–X(0,0) and A–X(1,1) bands and block background scattering. Both cameras employed a 512 × 512 pixel array that was binned to improve the framing rate.

To calibrate the Rayleigh scattering signal, images of the scattering intensity were taken of clean, particle-free air (at a known temperature) that was directed through the lower nozzle. Even though great care was taken to minimize the background scattering, some still existed. To account for this, high-purity helium was passed through the nozzles of the burner system, allowing the background to be measured. Helium was used for this purpose because its scattering cross section is very small compared to that of air (less than 1.5%). Also to account for any variations in the system (and minimize error) as the experiments were conducted, such as shifts in the laser sheet, the air-reference and background scattering were checked periodically.

To calibrate the intensity seen from the OH PLIF to an absolute number density of OH, measurements were first taken of a known system with the equivalent experimental arrangement. A 25.4-mm-square Hencken burner (see Ref. 24) using a premixture of methane and air (equivalence ratio of 0.95) was used as the calibration flame. Though there is a small difference in electronic quenching rate between this flame and that expected in the counterflow diffusion flames (due to the nitrogen in the fuel), the difference was mitigated due to transition saturation. The number density in the Hencken burner flame (in the burnt gas region) was determined with an absorption measurement, using the $Q_1(6)$ transition of the A–X(0,0) band, along with a LIF measurement of the absorption pathlength. This measurement gave an OH number density of (0.94 ± 0.07) × 10^{16} cm^{-3}, a value consistent with a burnt gas temperature of 2170 K (vs the adiabatic equilibrium value of 2194 K). The ratio of fluorescence signals between the counterflow flames and the Hencken burner flame, along with the number density in the Hencken burner flame, allowed for calculation of the counterflow flame number densities. A 10% correction factor was also applied to the Hencken burner flame fluorescence signals to account for the greater degree of fluorescence trapping and sheet absorption (compared to the counterflow flames); measured temperatures were used to correct the slight change in Boltzmann population fraction from Hencken burner to counterflow flames. The total fractional uncertainty for the counterflow OH number densities is estimated to be ±15%; this represents a combination of absorption measurement uncertainty and uncertainty of application of the calibration to the opposed flow flames.

III. Results and Discussion

This section is divided into four subsections describing experimental measurements of extinction limits, Rayleigh scattering for temperature profiles, OH PLIF for absolute OH number density, and numerical computations with radical addition. Numerical computations were performed using a modified version of PREMIX code[25] with both potential and plug flow boundary conditions and using the detailed chemical mechanism of GRI-3.0 (Ref. 26). The temperature input to the numerical computation came from the measured temperatures found just downstream of the exit of the nozzles via Rayleigh scattering thermometry for each of the various flow, concentration, and plasma power conditions.

A. Extinction Measurements

The extinction limits for the counterflow flames were found with and without plasma power addition. When the bypass valves were closed, the nozzle exit velocities increased, pushing the flame closer to the stagnation plane. As the flame approached the stagnation plane, the strain rate increased. The flame lost more heat and had less residence time for reaction completion until, finally, it extinguished. The effect of the stabilized piecewise nonequilibrium gliding arc plasma discharge on the extinction limits of the flame was observed. This was accomplished by using three different nitrogen-diluted methane mixtures, and the results can be seen in Fig. 8. The extinction limits with no plasma power addition agreed well with values reported by both Puri and Seshadri[19] and Bundy et al.[23] With only 78 W of plasma power input, there was a 220% increase in the extinction strain rate. This power input was less than 6% of the flame power, defined as the maximum power that could be obtained from the given amount of fuel in the mixture. These results showed that by using a stabilized piecewise nonequilibrium gliding arc plasma discharge there was a significant extinction limit enhancement, but the reasons for this effect were not yet apparent.

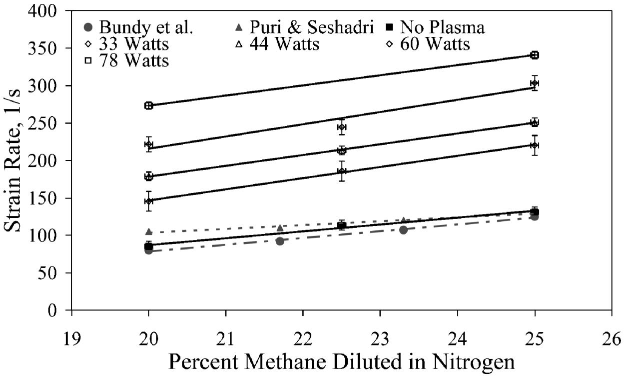

Fig. 8 Effects of plasma power addition on strain rates at extinction for different levels of nitrogen dilution.

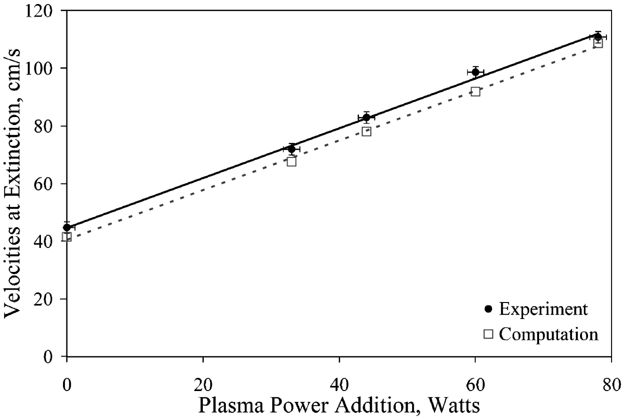

Fig. 9 Comparison of nozzle exit velocities at extinction.

To get an initial idea, the results for the extinction strain rates were then compared to that of the numerical computation. Because strain rate is proportional to velocity, the comparison was done in relation to velocities at extinction. The results can be seen in Fig. 9. Because the input to the computation was only elevated temperatures (obtained from the Rayleigh scattering, to be described in the next section) to mimic the plasma, and because both the experiment and computation extinction results are in good agreement, this gives an indication that the effect of the nonequilibrium plasma on the flame is predominately thermal.

B. Rayleigh Scattering

To measure quantitatively the temperature distribution and compare it with numerical simulations, Rayleigh scattering was performed on the counterflow flame for various strain rates. The laser sheet was passed through the diameter of the disk-shaped counterflow flame between the nozzles of the burner. Two sample images are shown with no plasma power addition (Fig. 10a) and with approximately 33 W of plasma power addition (Fig. 10b). The background has been subtracted and the air reference divided into each image. The intensity seen was both a function of scattering cross section and number density distributions between the nozzles. The scale below Fig. 10 shows the darkest for the least scattering and the highest temperature and the lighter for the most scattering and the lowest temperature. Therefore, the flame is located in the darkest region of these images just above the middle of the photograph, spanning the width. The nitrogen-diluted methane mixture is entering the field of view from the top of Fig. 10 and the air (plasma side) from the bottom. It is seen that even with the nonequilibrium plasma discharge,

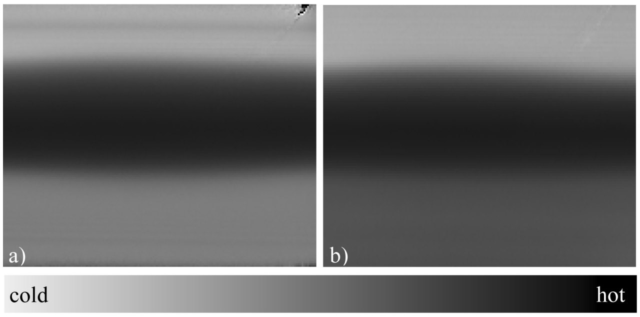

Fig. 10 **Rayleigh scattering images at a strain rate of 98.6 s^{-1}: a) no plasma power addition and b) 33-W plasma power addition.**

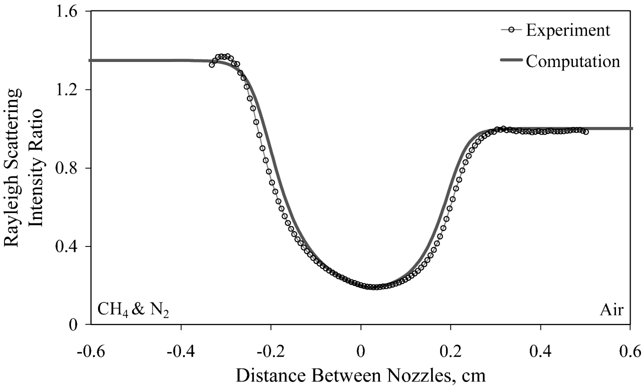

Fig. 11 **Comparison of Rayleigh scattering intensity ratio profiles with 0 W of plasma power addition at a strain rate of 87.1 s^{-1}.**

the present burner design yields a very good one-dimensional flame structure along the flow direction. This result greatly simplifies the coupling between the flowfield and the plasma–flame interaction. When comparing the two images, notice that the region below the flame in Fig. 10b (plasma on) is darker than Fig. 10a (plasma off) below the flame. This indicates less scattering and, hence, a higher temperature. In each case, a 10-pixel-wide “stripe” was taken from each image and averaged to yield the best distribution between the nozzles. The temperatures measured at the boundaries (just downstream of the nozzles) were then used as boundary conditions in the numerical computation.

1. *Rayleigh Scattering Intensity Ratio Profiles*

To get a better idea of how the flame was being enhanced by the nonequilibrium plasma, Rayleigh scattering thermometry was performed to obtain the distribution of temperature between the two nozzles. The intensity observed by the ICCD camera was a function of both the scattering cross section, because of the distribution of different species, and number density change between the two nozzles. By the simple referencing of those intensities to the intensity of air at room temperature, ratios were found. These measurements were then compared to that of numerical computation, and the results can be seen in Figs. 11–13 for both the plasma power off and on. Note that oscillations are evident in the scattering profiles, especially near the upper (fuel) nozzle; these resulted from diffraction from the edge of the absorptive filters used to clip the beam (and prevent scattering from the burner surfaces) and slight movement of the sheet between the measurements in the flame and of the air reference. Nonetheless, it can be seen that there is reasonably good agreement between the experiment and computation. This once again showed that the effect of the nonequilibrium plasma on the flame was predominately thermal.

2. *Temperature Profiles*

Even though the measurements directly from the Rayleigh scattering were in good agreement with the computation, and were also completely independent quantities, the actual temperatures were not realized. To then get a better idea of the temperatures, the ratio profiles as described earlier were used. Because the species concentrations and temperature changed between the nozzles due to the presence of the flame, the scattering cross sections and number densities changed. Number density could simply be accounted for by the temperature, but the scattering cross sections could not. Therefore, the scattering cross sections needed to be known at each point along the profile as a reference to derive the temperature. Therefore, the species concentrations associated with specific temperatures and axial positions from the numerical computation were used to convert scattering signal to temperature. The scattering cross sections for species in molar concentrations of 10ths of a percent and larger were calculated using refractory data from Gardiner et al.[27] This accounted for the variation in scattering cross section and gave accurate temperature profiles from the Rayleigh scattering. The temperature profiles found from the Rayleigh scattering were then compared to the results of the numerical computation at the same input temperatures and flow conditions. Figure 14 shows temperature profile comparisons between the experimental results via Rayleigh scattering and the numerical computation using the GRI-3.0 mechanism. The profiles are in good agreement. Figures 15 and 16 show similar comparisons between the experimental results and the numerical computation, except with the addition of plasma power. Once again, the temperature profiles are all in good agreement. Note that on the air side (the right-hand sides) is where the elevated temperature inputs were, mimicking the plasma. The air temperature was found experimentally from the Rayleigh scattering and given as the only input to the numerical computation. Overall, the temperature profiles agreed, therefore, once again showing that the effect of the nonequilibrium plasma can be seen as predominately thermal for the cases investigated.

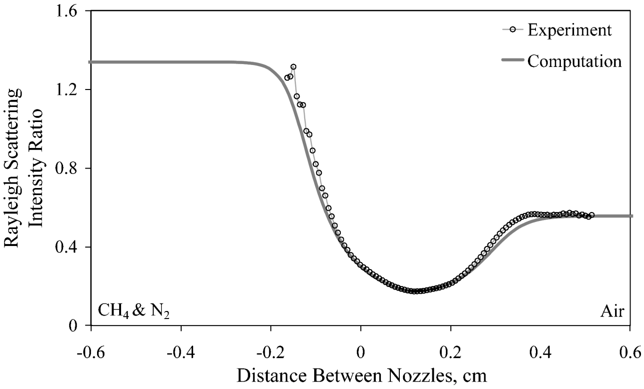

Fig. 12 **Comparison of Rayleigh scattering intensity ratio profiles with 33 W of plasma power addition at a strain rate of 98.6 s^{-1}.**

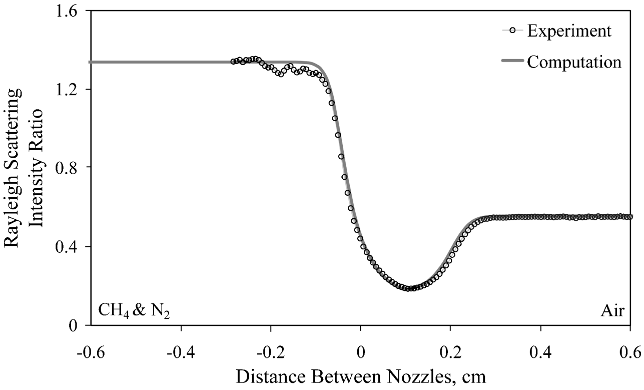

Fig. 13 **Comparison of Rayleigh scattering intensity ratio profiles with 60 W of plasma power addition at a strain rate of 298.5 s^{-1}.**

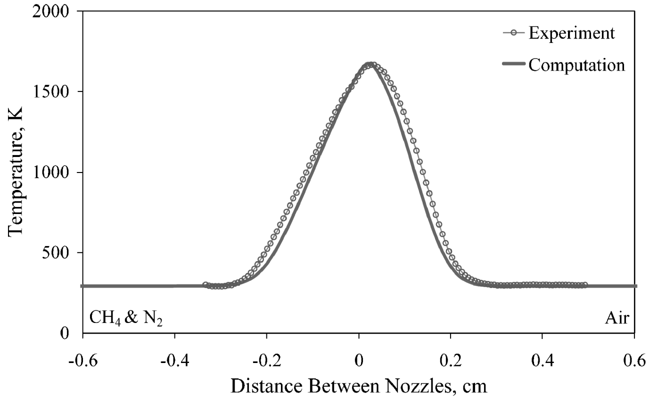

Fig. 14 Comparison of temperature profiles with 0 W of plasma power addition at a strain rate of 87.1 s^{-1}.

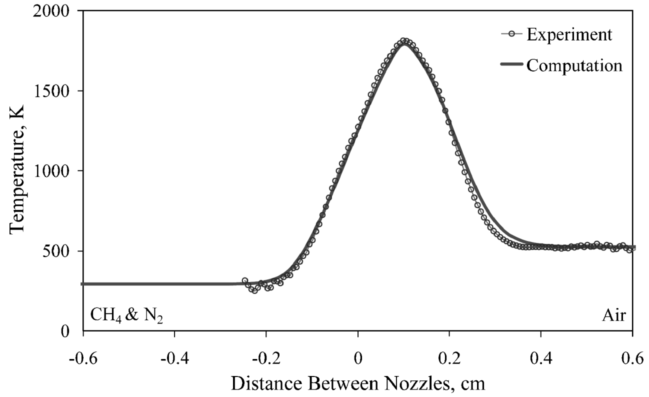

Fig. 15 Comparison of temperature profiles with 33 W of plasma power addition at a strain rate of 98.6 s^{-1}.

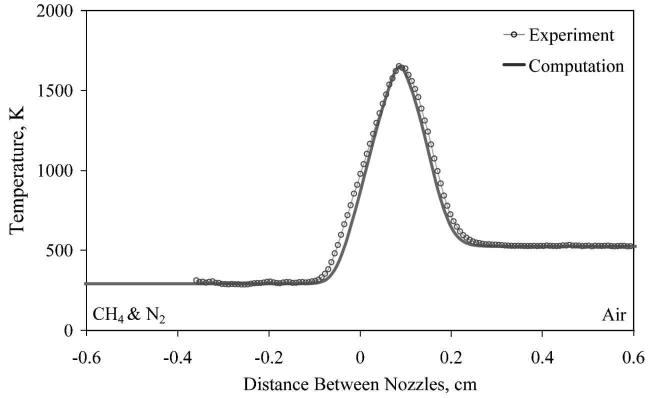

Fig. 16 Comparison of temperature profiles with 60 W of plasma power addition at a strain rate of 298.5 s^{-1}.

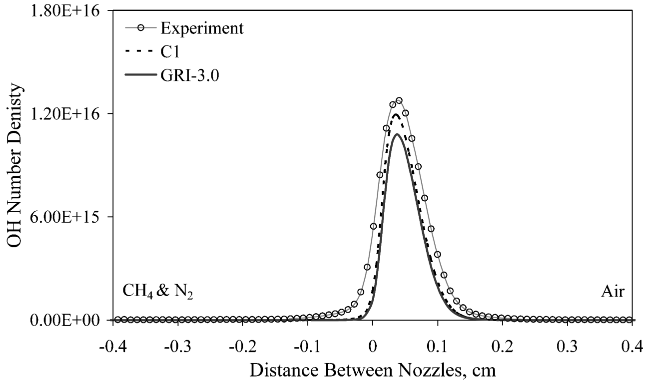

Fig. 17 Comparison of OH number density distributions with 0 W of plasma power addition at a strain rate of 83.3 s^{-1}.

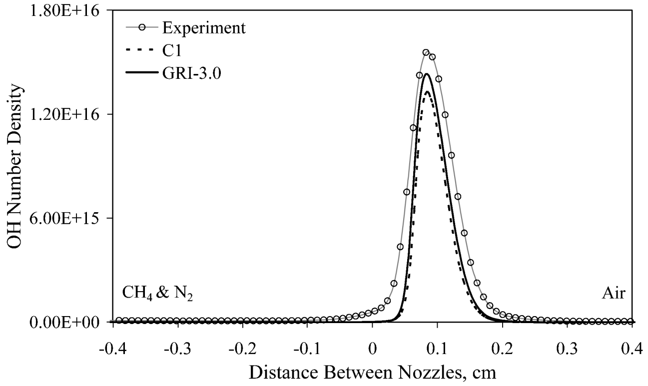

Fig. 18 Comparison of OH number density distributions with 48 W of plasma power addition at a strain rate of 183.0 s^{-1}.

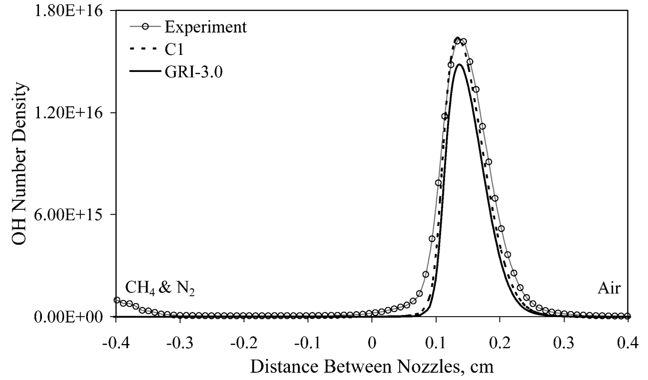

Fig. 19 Comparison of OH number density distributions with 78 W of plasma power addition at a strain rate of 127.7 s^{-1}.

C. OH PLIF

To further reinforce that the enhancement of the flame via the nonequilibrium plasma was dominated by thermal effects, OH PLIF measurements were performed. The OH number density was measured for different plasma powers and strain rates and referenced to a Hencken burner flame, as described earlier, to find the absolute OH number density. Figure 17 shows the results from the OH PLIF measurements when compared to the computation with no plasma power addition and Figs. 18 and 19 with plasma power addition. Note that the experimental profiles are consistently taller and broader than the computational profiles, but overall the agreement is within the uncertainty of the measurement, ±15%, as described earlier. Note also that because the 283-nm laser sheet was approximately 250 μm in width in the probe region (and transition saturation gives an effective probe thickness somewhat greater than this), one would expect a slight broadening of the experimental profiles. Nonetheless, Figs. 17–19 show reasonably good agreement between the experiment and the computation, therefore, once again showing that the effect of the nonequilibrium plasma on the flame is predominately thermal.

D. Radical Addition

What would be the lifetime of radicals produced by the plasma discharge in the airstream and would they reach the flame? This is reasonable to ask because, as observed, the effect appears to be predominately thermal, rather than nonthermal. Because the plasma is only activating dry air, it can be assumed that the radicals produced in the flame will only consist of oxygen and nitrogen. Here, only the effect of oxygen atom addition at the air side boundary on the flame structure will be shown (once again mimicking the plasma)

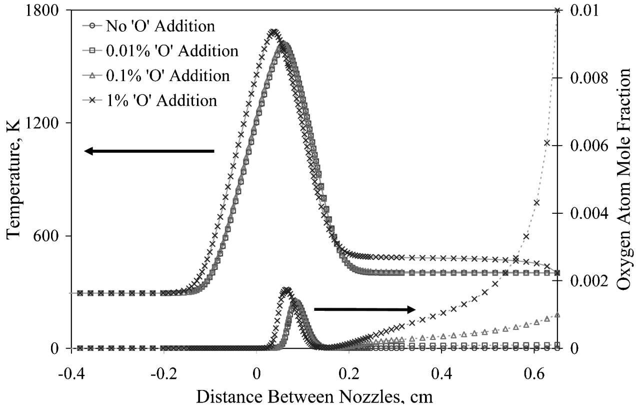

Fig. 20 Computed temperature and oxygen atom distributions between nozzles of counterflow system with oxygen atom addition.

because the nitrogen atom addition plays a similar role. Oxygen atom concentrations from 0.01 to 1% were added at the air (plasma) side boundary. The temperature was fixed at 400 K at this boundary to ensure that low-temperature chemistry did not come into play. Also, the velocities at the boundaries were similar to those used in the experiment for a flame that is highly strained and near extinction, where radical addition may be important. The temperature profiles and oxygen atom concentration distributions between the nozzles can be seen in Fig. 20. It is shown that there is no significant effect until almost 1% oxygen atom addition. When it is considered that the plasma disk is located almost 4 cm upstream of this boundary where the oxygen atoms were added, it appears that these atoms will recombine well before the flame, therefore, having no nonthermal effect on the flame.

From the preceding discussion, we can conclude that the radical-induced nonthermal effects on the burning rate of diffusion flames are very limited at low air temperatures because the radical lifetime is too short to affect the chain branching reaction path. The oxygen radicals simply recombine and increase the air temperature before reaching the flame. In addition, the low temperature of air excludes the occurrence of the low-temperature chemistry. Future experiments to observe the nonthermal plasma–flame interaction should be conducted at reduced pressures and elevated air temperatures so that the radical lifetime can be extended and low-temperature fuel oxidation chemistry can be involved.

IV. Conclusions

A new stabilized piecewise nonequilibrium gliding arc plasma discharge system was developed and validated for the study of nonequilibrium plasma–flame interaction by integrating it with a counterflow burner. Experiments showed that the present system yields a well-defined one-dimensional flame structure. The excellent agreement between laser diagnostics of temperature and OH radical distributions with numerical simulations confirmed that the present plasma discharge system provides an ideal platform to study the mechanism of the nonequilibrium plasma–flame interaction. Experimental results of a low-power plasma discharge in the airstream showed that a plasma discharge could significantly increase the extinction limits of the diffusion flame at low-power input. Direct comparisons of the extinction limits and temperature and OH distributions between the experiment and numerical simulations demonstrated that the combustion enhancement at a low-power discharge in the airstream was dominated by thermal effects, that is, heating of the airstream. Numerical computations with oxygen radical addition in the airstream confirmed this conclusion. The results also showed that the lack of the nonthermal effect on the flame burning limit at low-power discharge was caused by the fast recombination of active radicals. Future experiments to observe nonthermal enhancement of combustion via the plasma–flame interaction needs to be conducted at elevated air temperatures or reduced pressures.

Acknowledgments

This work was graciously supported by the Air Force Office of Scientific Research under Contract F49620-04-1-0038. Also, Yiguang Ju thanks the Air Force Research Laboratory and the National Science Foundation under Grant CTS-0418403 for support for the laser diagnostic equipment.

References

[1] Gruber, M. R., Baurle, R. A., Mathur, T., and Hsu, K.-Y., "Fundamental Studies of Cavity-Based Flameholder Concepts for Supersonic Combustors," *Journal of Propulsion and Power*, Vol. 17, No. 1, 2001, pp. 146–153.

[2] Gruber, M. R., Donbar, J. M., Carter, C. D., and Hsu, K.-Y., "Mixing and Combustion Studies Using Cavity-Based Flameholders in Supersonic Flow," *Journal of Propulsion and Power*, Vol. 20, No. 5, 2004, pp. 769–778.

[3] Yu, K. H., Wilson, K. J., and Schadow, K. C., "Effect of Flame-Holding Cavities on Supersonic-Combustion Performance," *Journal of Propulsion and Power*, Vol. 17, No. 6, 2001, pp. 1287–1295.

[4] Yu, G., Li, J. G., Chang, X. Y., Chen, L. H., and Sung, C. J., "Fuel Injection and Flame Stabilization in Liquid-Kerosene-Fueled Supersonic Combustor," *Journal of Propulsion and Power*, Vol. 19, No. 5, 2003, pp. 885–893.

[5] Yu, G., Li, J. G., Zhang, X. Y., Chen, L. H., Han, B., and Sung, C. J., "Experimental Investigation on Flameholding Mechanism and Combustion Performance in Hydrogen-Fueled Supersonic Combustors," *Combustion Science and Technology*, Vol. 174, No. 3, 2002, pp. 1–27.

[6] Guerra, R., Waidmann, W., and Laible, C., "An Experimental Investigation of the Combustion of a Hydrogen Jet Injected Parallel in a Supersonic Air Stream," AIAA Paper 91-5102, Dec. 1991.

[7] Ju, Y., and Niioka, T., "Ignition Simulation of Methane/Hydrogen Mixtures in a Supersonic Mixing Layer," *Combustion and Flame*, Vol. 102, No. 4, 1995, pp. 462–470.

[8] Tabejamaat, S., Ju, Y., and Niioka, T., "Numerical Simulation of Secondary Combustion of Hydrogen Injected from Preburner into Supersonic Airflow," *AIAA Journal*, Vol. 35, No. 9, 1997, pp. 1441–1447.

[9] Takita, K., "Ignition and Flame-Holding by Oxygen, Nitrogen and Argon Plasma Torches in Supersonic Airflow," *Combustion and Flame*, Vol. 128, No. 3, 2002, pp. 301–313.

[10] Takita, K., Moriwaki, A., Kitagawa, T., and Masuya, G., "Ignition of H_2 and CH_4 in High Temperature Airflow by Plasma Torch," *Combustion and Flame*, Vol. 132, No. 4, 2003, pp. 679–689.

[11] Bozhenkov, S. M., Starikovskaia, S. M., and Starikovskii, A. Yu., "Nanosecond Gas Discharge Ignition of H_2- and CH_4 Containing Mixtures," *Combustion and Flame*, Vol. 133, No. 1-2, 2003, pp. 133–146.

[12] Starikovskaia, S. M., Kukaev, E. N., Kuksin, A. Y., Nudnova, M. M., and Starikovskii, A. Y., "Analysis of the Spatial Uniformity of the Combustion of Gaseous Mixture Initiated by Nanosecond Discharge," *Combustion and Flame*, Vol. 139, No. 3, 2004, pp. 177–187.

[13] Chintala, N., Meyer, R., Hicks, A., Bystricky, B., Rich, J. W., Lempert, W. R., and Adamovich, I. V., "Non-Thermal Ignition of Premixed Hydrocarbon–Air and CO–Air Flows by Non-Equilibrium RF Plasma," AIAA Paper 2004-0835, Jan. 2004.

[14] Sullivan, D., Zaidi, S. H., Macheret, S. O., Ju, Y., and Miles, R. B., "Microwave Techniques for the Combustion Enhancement of Laminar Flames," AIAA Paper 2004-3713, July 2004.

[15] Zaidi, S., Macheret, S., Vasilyak, L., Miles, R., and Ju, Y., "Increased Speed of Premixed Laminar Flames in a Microwave Resonator," AIAA Paper 2004-2721, June–July 2004.

[16] Kalra, C., Gutsol, A., and Fridman, A., "Gliding Arc Discharges as a Source of Intermediate Plasma for Methane Partial Oxidation," *IEEE Transactions on Plasma Science*, Vol. 33, No. 1, 2005, pp. 32–41.

[17] Kuznetsova, I. V., Kalashnikov, A. F., Gutsol, A. F., Fridman, A. A., and Kennedy, L. A., "Effect of 'Overshooting' in the Transitional Regimes of the Low-Current Gliding Arc Discharge," *Journal of Applied Physics*, Vol. 92, No. 8, 2002, pp. 4231–4237.

[18] White, F., *Viscous Fluid Flow*, McGraw–Hill, New York, 1974, pp. 204–208.

[19] Puri, I. K., and Seshadri, K., "Extinction of Diffusion Flames Burning Diluted Methane and Diluted Propane in Diluted Air," *Combustion and Flame*, Vol. 65, No. 2, 1986, pp. 137–150.

[20] Maruta, K., Yoshida, M., Guo, H., Ju, Y., and Niioka, T., "Extinction of Low-Stretched Diffusion Flame in Microgravity," *Combustion and Flame*, Vol. 112, No. 1-2, 1998, pp. 181–187.

[21] Seiser, R., Seshadri, K., Piskernik, E., and Linan, A., "Ignition in the Viscous Layer Between Counterflowing Streams: Asymptotic Theory with Comparison to Experiments," *Combustion and Flame*, Vol. 122, No. 3, 2000, pp. 339–349.

[22] Humer, S., Seiser, R., and Seshadri, K., “Non-Premixed and Premixed Extinction and Autoignition of C_2H_4, C_2H_6, C_3H_6, C_3H_8,” *Proceedings of the Combustion Institute*, Vol. 29, 2002, pp. 1597–1604.

[23] Bundy, M., Hammins, A., and Lee, K. Y., “Suppression Limits of Low Strain Rate Non-Premixed Methane Flames,” *Combustion and Flame*, Vol. 133, No. 3, 2003, pp. 299–310.

[24] Barlow, R. S., Karpetis, A. N., Frank, J. H., and Chen, J.-Y., “Scalar Profiles and NO Formation in Laminar Opposed-Flow Partially Premixed Methane/Air Flames,” *Combustion and Flame*, Vol. 127, No. 3, 2001, pp. 2102–2118.

[25] Ju, Y., Guo, H., Maruta, K., and Liu, F., “On the Extinction Limit and Flammability Limit of Non-Adiabatic Stretched Methane–Air Premixed Flames,” *Journal of Fluid Mechanics*, Vol. 342, 1997, pp. 315–334.

[26] Smith, G. P., Golden, D. M., Frenklach, M., Moriarty, N. W., Eiteneer, B., Goldenberg, M., Bowman, C. T., Hanson, R. K., Song, S., Gardiner, W. C., Jr., Lissianski, V. V., and Qin, Z., GRI-Mech Homepage, Gas Research Inst., Chicago, URL: http://www.me.berkeley.edu/gri_mech/ [cited 20 December 2004].

[27] Gardiner, W. C., Jr., Hidaka, Y., and Tanzawa, T., “Refractivity of Combustion Gases,” *Combustion and Flame*, Vol. 40, 1981, pp. 213–219.

R. Lucht
Associate Editor

Color reproductions courtesy of the U.S. Air Force Research Laboratory.